Check for updates

Original article

Institution of MECHANICAL ENGINEERS
Journal of PROCESS MECHANICAL ENGINEERING

Proc IMechE Part E:
J Process Mechanical Engineering
1–14
© IMechE 2025
Article reuse guidelines:
sagepub.com/journals-permissions
DOI: 10.1177/09544089251324547
journals.sagepub.com/home/pie
Sage

Investigation of dynamic recrystallization induced surface integrity in cryogenic machining of AISI 316LVM stainless steel

Emin Ozdemir[1] and Abdulkadir Gullu[2]

Abstract

This study addresses the effects of cryogenic cooling-induced severe plastic deformation (SPD) on microstructure alteration and dynamic recrystallization in the machining of 316LVM alloy. In particular, surface integrity properties such as nanocrystallization, phase transformation, and deformation hardening in the subsurface layer were experimentally investigated. Machining was carried out under liquid nitrogen cooling with cutting parameters consisting of a cutting speed of 300 m/min, a depth of cut of 1.2 mm, and two different feedrates (0.1 and 0.5 mm/rev). An SPD layer with a thickness of approximately 27 to 38 μm and a featureless layer with a thickness of 6 μm were detected in the subsurface of the sample machined at the high feedrate. Furthermore, nanostructures with grain features averaging 93 nm in size were observed in the featureless layer using an atomic force microscope. As a result of X-ray diffraction analysis, while no deformation-induced martensitic phase transformation was observed in the nanocrystal surface layer, a 338% peak broadening was detected. Due to work-hardening, microhardness increased by 115%, reaching 516 HV at a depth of 10 μm in the subsurface. It is thought that the nanocrystallization occurring in the 316LVM alloy with high stacking fault energy results from continuous dynamic recrystallization induced by SPD.

Keywords

316LVM, surface integrity, dynamic recrystallization, microstructure, microhardness, phase transformation

Date received: 10 November 2024; accepted: 10 February 2025

Introduction

Austenitic stainless steels have been used in various industrial applications and the medical field due to their excellent properties such as high strength, ductility, biocompatibility, corrosion resistance, and good formability. In addition to the production of internal fixation devices used in orthopedic surgery and stents used in cardiovascular surgery, it is preferred in the medical field as an affordable alternative to titanium and cobalt–chromium alloys in manufacturing surgical implants.[1] AISI 316LVM austenitic stainless steel, which has replaced the AISI 316L alloy in implant production in recent years, is called medical quality.[2] While the surface layer of biomedical implants and other critical structural components used in the industry are desired to be hard and have high strength values, the interior parts are desired to be ductile and tough. The combined effects of controllable ultra-fine/nano-grain structures and strain hardening created by severe plastic deformation (SPD) on the machined surface and subsurface of metals provide improvements in the functional properties of the components, such as fatigue strength, wear resistance, corrosion resistance, and tribological behavior.[3–6] However, it has been reported in the literature machining is regarded as an effective method to improve functional performance by forming a nano/ultrafine grain structure on the surface.[3–5] Machining, especially applied under specific cooling and cutting conditions, is categorized as an SPD process due to its high strain (typically ~2–10), high strain rate (106 s^{-1}), and high-temperature conditions.[3,4,7] Dynamic recrystallization (DRX) has been reported as the grain refinement mechanism in machining and other SPD processes.[3–5,7,8]

DRX mechanisms such as rotational dynamic recrystallization (RDRX),[9] discontinuous dynamic recrystallization (DDRX), and continuous dynamic recrystallization (CDRX)[10–12] occuring in various metallic materials under different thermomechanical processing conditions have been mentioned in the literature. In addition, it has been explained in many studies that the grain refinement

[1]Department of Engineering Sciences, Istanbul University-Cerrahpaşa, Istanbul, Turkiye
[2]Department of Manufacturing Engineering, Gazi University, Ankara, Turkiye

Corresponding author:
Emin Ozdemir, Department of Engineering Sciences, Istanbul University-Cerrahpaşa, 34320 Avcilar, Istanbul, Turkiye.
Email: emin.ozdemir@iuc.edu.tr

Table 1. Chemical composition of AISI 316LVM workpiece (wt.%).[20]

Element	C	Cr	Ni	Mo	Mn	Si	Cu	N	P	S
wt.%	0.016	17.509	14.697	2.748	1.799	0.432	0.07	0.076	0.018	0.002

mechanism in machining processes occurs through DRX and effective cooling.[4,7,13,14] Ni et al.[13] reported that DRX formed in the microstructure due to the machining of Al 1100 alloy with face-centered cubic (FCC) structure and medium-high stacking fault energy (SFE) value under cooling liquid. It was stated that the average grain size was 360 nm due to the restriction of grain growth by the cutting fluid. Wusatowska-Sarnek et al.[14] stated that the ultra-fine microstructure of the white etched layer, which exhibits nanostructure character after the machining process of a fine-grained IN100 Ni-based superalloy, consisting of new nanoparticles of 15 to 70 nm in size, is due to DRX. It has been explained that grain refinement is a result of one-step CDRX, in which grain boundary migration is prevented due to the high deformation rate and short cooling times. Considering the above explanations as well as the Hall–Petch and Zenner–Holloman equations,[11,15–17] control of the deformation temperature is effective on grain refinement and work-hardening. In recent years, environmentally friendly cryogenic liquid nitrogen (LN_2) has been used instead of conventional cutting fluids for effective cooling in machining.[3,18,19] It has been reported that cryogenic LN_2 cooling applied during the machining of AISI 304 austenitic stainless steel cools the machined surface very rapidly, preventing the dynamic recovery of the microstructure and causing the formation of a nanocrystalline white layer in the subsurface.[4] Pu et al.[7] reported with atomic force microscope (AFM) images that a nanolayer with a grain size of 31 nm was formed as a result of RDRX in the subsurface of the sample exposed to SPD during the machining of AZ31B Mg alloy under cryogenic LN_2.

This study aims to investigate the microstructural alteration and DRX occurring in the subsurface layer, which significantly affects the service performance of medical implants produced from biomedical grade austenitic stainless steel alloy AISI 316LVM. Although few in the literature, DRX has been studied in previous research in machining with different materials such as AZ31B Mg,[7] Al 1100,[13] and IN100.[14] However, no study has been found in the literature investigating the formation of DRX during the machining process in austenitic stainless steels, which have always been an essential model alloy for DRX research in recent years. Additionally, numerous studies have been conducted to determine the effects of cryogenic machining on cutting tool life and machining performance.[3,18,19] However, the number of studies on surface integrity is quite limited. Therefore, this study investigates DRX formations in the subsurface layer exposed to SPD caused by machining under cryogenic LN_2 cooling, which has attracted the attention of researchers in recent years, in AISI 316LVM austenitic stainless steel. Additionally, surface integrity characterizations such as nanocrystallization, phase transformation, and deformation hardening affected by DRX, as well as relationships between them, were investigated theoretically and experimentally. The expected outcome of this study is to contribute to the development of functional performance in medical implants by obtaining the desired surface integrity characteristics such as microstructure, grain size, microhardness, and phase transformation on the surface and subsurface of components produced by machining in the medical implant industry without requiring additional processes and costs.

Experimental setup and procedure

Material

Medical-grade AISI 316LVM steel, one of the hot-rolled austenitic stainless steel alloy produced by Ugitech (France), was used in the experiments. An AISI 316LVM stainless steel bar with a diameter of 30 mm is delivered in annealed form and is prepared in line with the ISO 5832.1 standard. Table 1 shows the chemical composition of the workpiece material. The thermal conductivity of AISI 316LVM material is 16.3 W/(mK).[20] In the microstructure of AISI 316LVM seen in Figure 1, which consists entirely of FCC austenite (γ), shear bands (black arrows) within the austenite grains appear alongside the intense annealing twins (yellow arrows) caused by hot rolling. The average grain size of the as-received material was calculated as 16.80 μm.[21]

Machining test

The workpiece with a diameter of Ø30 mm and a length of 30 mm were machined under LN_2 cooling with cutting parameters consisting of 300 m/min cutting speed, 1.2 mm depth of cut, and two different feedrates (0.1 mm/rev and 0.5 mm/rev). One experiment was conducted for each machining condition. In the experiments, TM4000 grade, Ti(C, N) + AL_2O_3 CVD coated CNMG120408-MF4 carbide inserts with 0.8 mm nose radius produced by SECO were employed. Cutting parameters were fixed by taking into account the values recommended by the cutting tool manufacturer SECO,[22] literature,[23–27] and preliminary experiments. A PCLNL2525M12JET tool holder with a 95° tool cutting edge angle, a −6° normal rake angle, and a −6° inclination angle was employed. The machining experiment was performed on a Johnford TC-35 CNC lathe. Cryogenic LN_2 stored at −196 °C and under 15 bar pressure was sprayed onto the rake and flank faces of the

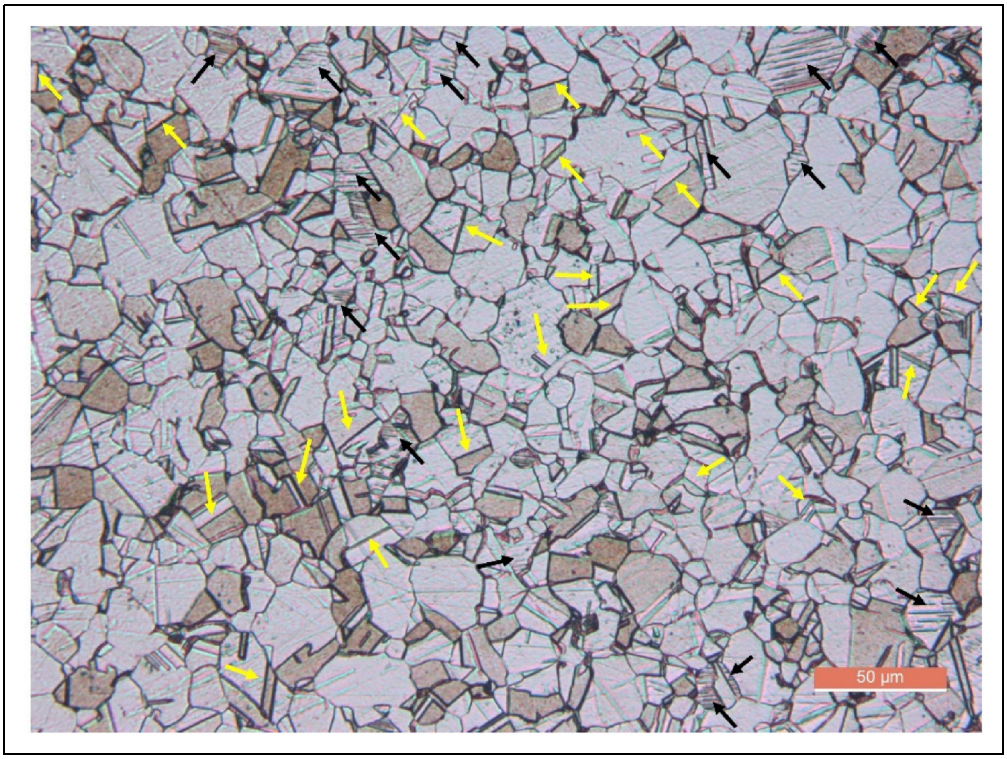

Figure 1. As-received AISI 316LVM bulk material microstructure.

cutting tool to cool the cutting region via three internal cooling nozzles of the tool holder with diameter of 1 mm (Figure 2(a) and (b)).

Measurements

The cutting forces were measured using a Kistler 9257B-type piezoelectric dynamometer. The cutting temperature during machining was continuously monitored by the Raytek MI3 infrared non-contact temperature meter (pyrometer), which can measure in the range of 250–1400 °C and has an accuracy of ±0.5% at a +2 °C reading. The emissivity of the pyrometer was set to 0.6.[23] Using a data connection and USB, the pyrometer sensor, mounted on the CNC lathe turret at a distance of 30 cm from the cutting tool tip and the laser beam focused on the cutting tool tip, detected the temperatures (Figure 2(c)). Tool wear was evaluated with images of the cutting edge from the flank face and nose taken with a digital microscope (Dino-Lite AM4113T).

In this study, in addition to BUE formations, significant flank and nose wear due to high feedrate at 0.5 mm/rev was observed in cutting tools used in machining tests (Figure 5). It is generally known that BUE develops on the cutting tool at low cutting speeds when carbon steels are being machined; when cutting speed is increased, the cutting process gets simpler and BUE formation is reduced.[28] However, because austenitic stainless steel alloys have a more ductile structure than carbon steels, they are more susceptible to chip adhesion and tool wear during the machining process.[28,29] BUE occurring on the cutting edges is formed as a result of material adhesion with the effect of the adhesive wear mechanism.[29] BUE formation, which generally occurs at low and medium cutting speeds in dry cutting conditions of austenitic stainless steels, occurred at a high cutting speed of 300 m/min with the effect of cryogenic LN_2 cooling.[23]

Microstructure and x-ray diffraction analyses

Microstructure, microhardness, and phase transformation analyses of the surface and subsurface layers of the specimens were performed. The analysis samples were cut to the required dimensions without causing any changes in the microstructure and were subjected to grinding and polishing processes after molding. The specimen was etched for 5 minutes with a solution containing 3% glycerin + 5% HCl + 1% HNO_3 prepared for AISI 316LVM material. The subsurface microstructure of the sample was imaged with a Leica DM 4000M optical microscope. The featureless SPD layer was re-imaged in the JEOL JSM 6060 LV scanning electron microscope (SEM) device. Microstructure grain sizes were calculated with ImageJ 1.52a software according to the intercept method in the ASTM-E112 standard.[21] AFM device was used for the microstructure analysis of the featureless SPD layer, whose grain boundaries could not be visualized in the SEM device since good results were previously reported in the literature.[7,30,31] The 2×2 μm^2 reference area within the featureless SPD layer was investigated and imaged using a commercial silicon cantilever system (Nanosensors, type: PPP-NCL-50) with a constant force of approximately 50 N/m at a resonance frequency

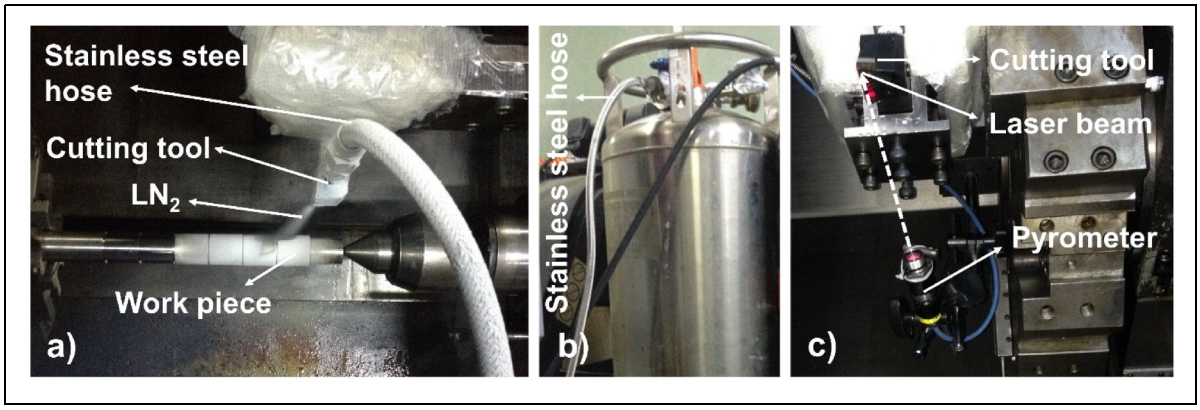

Figure 2. Experimental setup: (a) cryogenic turning operation, (b) LN_2 tank, and (c) pyrometer position.

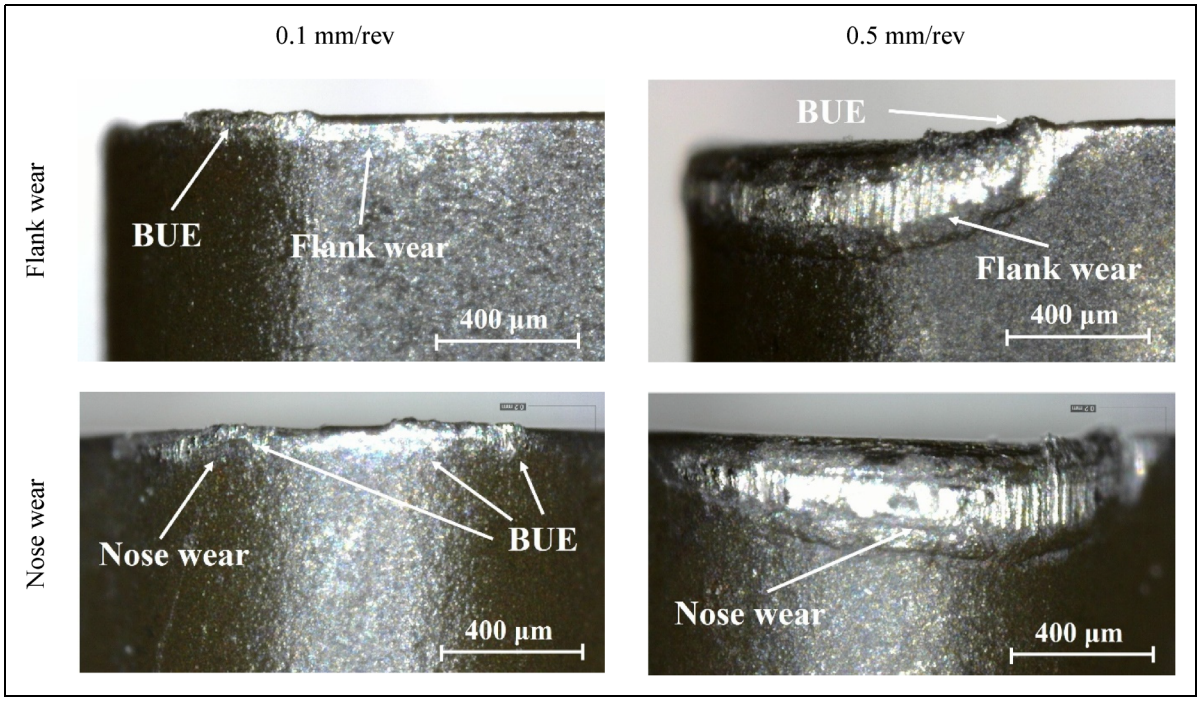

Figure 5. Images of tool wear.

of 161 kHz, in tapping mode, at nanoscale and high resolution on a NanoMagnetics Instruments brand AFM device.

Microhardness changes in the subsurface layer of the sample were measured with a SHIMADZU brand HMV-2 Vickers hardness tester. Microhardness was measured by applying a load of 245 mN (HV 0.025) for 15 seconds at a depth of 10 µm from the machined surface. The average of the measurements made in three repetitions was taken.

As reported in similar studies in the literature,[6–8,31,32] X-ray diffraction (XRD) measurements were carried out to analyze grain refinement, deformation hardening, and phase transformation on the machined surfaces. The MATCH software was used to digitize the diffraction patterns obtained in the GNR APD 2000 PRO brand XRD device. The scanning was carried out with 0.1 step size between 40° and 80° 2θ angles, using Cu Kα cathode with a wavelength of 1.54060 Å.

Results and discussions

Microstructure characterization

Microstructure images of the subsurface layers of the machined samples viewed with an optical microscope are presented in Figure 3. It has been observed that SPD induced by machining performed at a high cutting speed of 300 m/min under cryogenic cooling has a significant effect on the subsurface microstructure of the machined samples. It was determined that an approximately 3.5 to 5.5 µm thick SPD layer was formed at a feedrate of 0.1 mm/rev, while an approximately 27 to 38 µm thick SPD layer was formed at a high feedrate of 0.5 mm/rev.

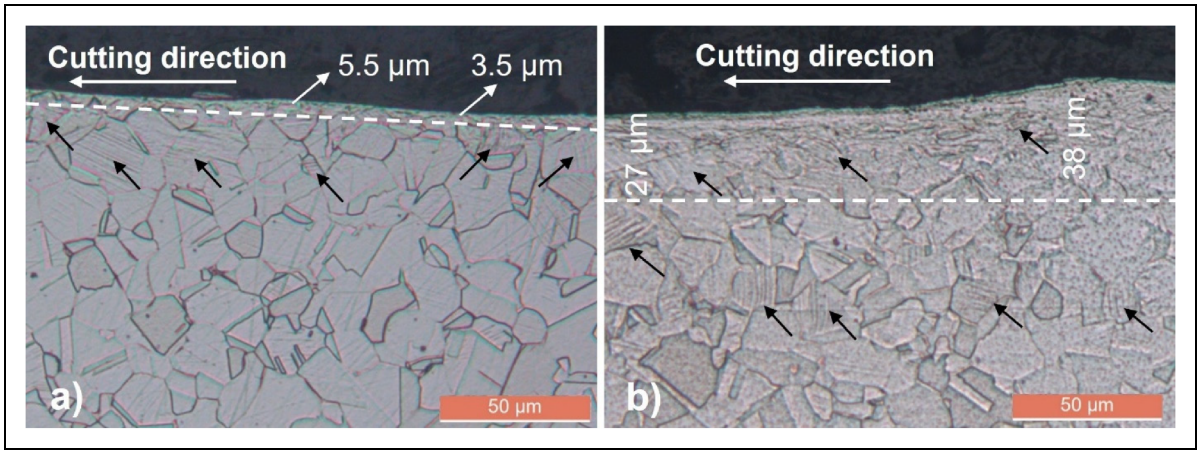

Figure 3. Optical microscope image of the subsurface microstructure of the machined sample (the black arrows point to shear bands): (a) 0.1 mm/rev and (b) 0.5 mm/rev.

While high cutting speed causes the formation of an SPD layer under the machined surface, it has been observed that the thickness of the SPD layer increases with increasing deformation along with the feedrate. As previously reported by Klocke et al.,[4] the high radial force (560 N at Figure 4(a)) caused by the high feedrate (0.5 mm/rev) increased the penetration depth of the SPD layer. A similar situation in which the SPD layer increases with a high feedrate has been previously reported in the literature.[32]

The thick SPD layer visible in Figure 3(b) can be attributed to the SPD caused by aggressive cutting parameters such as cryogenic LN_2 cooling, high cutting speed, and high feedrate, as well as the ploughing effect of nose wear on the cutting tool (Figure 5). Klocke et al.[4] have previously reported the ploughing effect causes compression of the material and deep plastic deformation. The boundaries of the grains that were elongated in the cutting direction due to SPD disappeared as they approached the machined surface. It is stated in the literature that on the surface where grain refinement occurs as a result of the cryogenic process, the grains first elongate with simultaneous tensile stress and compressive stress.[6] In addition to all these, when compared to the microstructures of both the as-received material in Figure 1 and the sample machined at a feedrate of 0.1 mm/rev, it was observed that the shear bands (pointed by the black arrows in Figure 3) in the microstructure increased as a result of 0.5 mm/rev high federate induced SPD. This microstructure alteration occurring under the surface has been attributed to thermomechanical effects such as high cutting tool pressure and high heat generation occurring during machining.[33] A similar situation has been previously reported in the literature for 316L material subjected to deformation.[34]

The thick SPD layer in Figure 3(b) was examined in more detail with SEM and AFM devices to visualize the microstructure features better, and the results are presented in Figure 6. In the SEM image of the thick SPD layer in Figure 6(c), a featureless layer with a thickness of 6 µm was detected, where distinct grain structures and boundaries were completely absent. No grain structure was found in the enlarged image of this featureless layer presented in Figure 6(a). This situation is thought to be caused by nanoscale ultra-fine grain formations that occur due to DRX and whose structures cannot be visualized under this magnification. It has also been reported in other studies in the literature that the high strain rate ($>10^6$ s^{-1}) in the machining process and the high strains caused by the low cutting temperature resulting from cryogenic application create an SPD layer with a very fine grain size at the nanoscale.[6,7,13] Therefore, significant grain refinement in the subsurface layer is expected due to SPD due to cryogenic cooling, high cutting speed, and high feedrate compared to the as-received bulk material average grain size (16.8 µm). In addition, in previous studies where stainless steels and other materials were deformed, tapping-mode AFM was reported to successfully provide grain boundary details in nanostructures.[6,30,31,35] It was claimed by Pang et al.[35] that the result of tapping-mode AFM grain size measurement is quite similar to the TEM (transmission electronic microscopy) measurement and the difference between them is only 10%. In line with this information, as a result of examining the image of the featureless layer obtained with the AFM device in Figure 6(b), nanoscale structures showing grain properties were detected. The average size of the grain-like structures in this featureless layer, whose AFM image is presented in Figure 6(b), was calculated to be 93 nm using the ImageJ 1.52a software and according to the intercept method in the ASTM-E112 standard.[21] Since grains smaller than 100 nm are considered nano-sized grains, this featureless SPD layer of µm thickness in Figure 6(c) is called a "nanolayer" acording to the literature.[4] This result obtained from Figure 6 is in agreement with the findings regarding nanocrystalline grains formed as a result of the DRX in the subsurface layer as a result of the high strain rate deformation of copper, titanium, and tantalum alloys,[9] low and high-speed

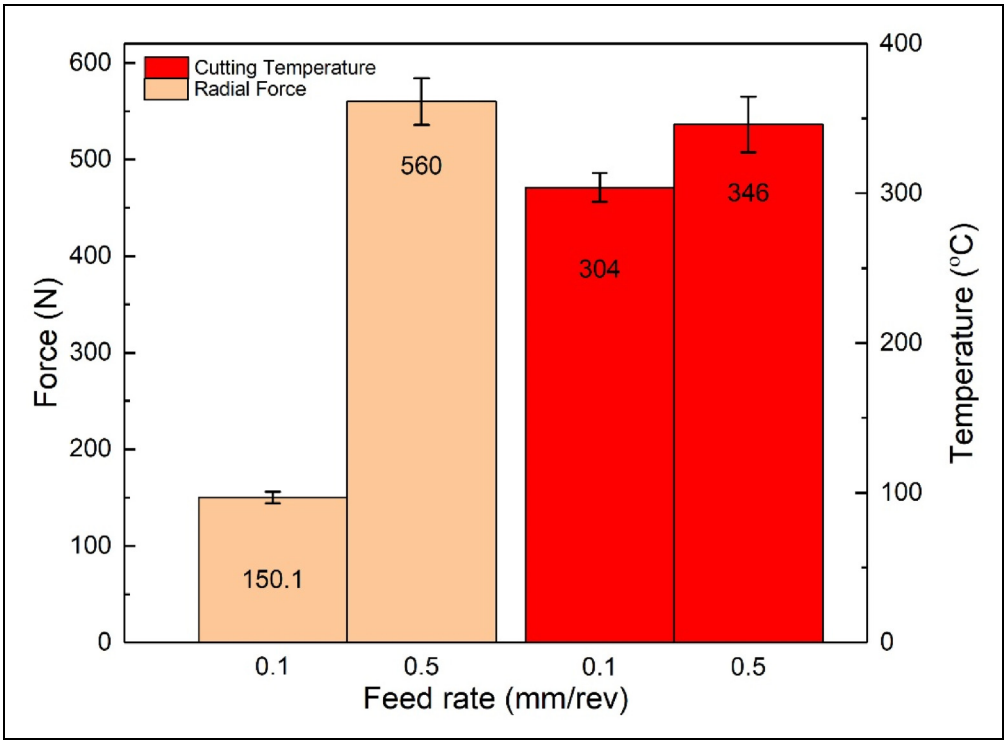

Figure 4. Radial cutting force and cutting temperature.

deformation of AISI 304 alloy,[10] high-pressure torsion test of AISI 316 alloy,[36] hot torsion deformation test of AISI 304 alloy,[11] equal-channel angular extrusion process of the 1421Al alloy,[12] and machining of the AZ31B Mg[7] and Al 1100 alloys.[13]

The microstructural features of the nanolayer seen in Figure 6 may be subgrains and high-density dislocation arrays forming subgrain boundaries as reported in the literature.[37] The literature elucidates that DRX is the primary mechanism behind grain refinement. Furthermore, during high-temperature plastic deformation, the dislocation arrays that establish high-energy subgrain boundaries function as nucleation sites, contributing to the formation of subgrains and, consequently, new grains.[4] In processes applied at high strain rates (>106 $s^{-}1$), such as machining, deformation occurs only by dislocation movement as there is not enough time for grain boundary sliding, even if the deformation temperature is high.[15] In addition, it has been stated in the literature that new ultra-fine grains can be formed in the microstructure due to the CDRX mechanism, which occurs independently of SFE, due to SPD induced by the cold or warm deformation process such as cryogenic machining. Because the dislocation sub-boundaries formed at low strains progressively turn into ultra-fine grains with high-angle boundaries at high strains.[16] As a result, based on the available findings and literature, in this study, it is thought that CDRX is the mechanism that causes the grain size to decrease dramatically to the nanoscale in the subsurface of the AISI 316LVM alloy with high SFE. It has been stated in previous studies that CDRX occurs as a result of the formation of new grains with high-angle grain boundaries by progressive rotation of subgrains (RDRX).[9,15] However, although this process, which gradually evolves into high-angle grain boundaries with the increase in deformation, has been reported as CDRX, the process may transition from DDRX to CDRX due to the effect of thermomechanical process conditions or change in initial grain size.[15]

It is understood from the above explanations that a critical strain (ε_c) and temperature (T) must be provided for the DRX process to start in the AISI 316LVM alloy. The critical strain (ε_c) expressed in Eq. (1) [17] is a strain slightly lower than the peak strain (ε_p) corresponding to the maximum peak stress (σ_P) on the flow curve in the stress–strain diagram of the material. Below this critical deformation value, where recrystallization does not occur, only dynamic recovery occurs. It is seen below that the peak strain (ε_p), as expressed in Eq. (2),[17] and, accordingly the critical strain (ε_c), expressed in Eq. (1), are a function of the Zener–Hollomon parameter (Z).[17]

$$\varepsilon_c = A \cdot \varepsilon_p \tag{1}$$

$$\varepsilon_p = A \cdot Z^p \cdot D_0^m \tag{2}$$

where D_0 is the initial grain size, A, m, and p are the material coefficients in the equations, and it has been reported in the literature that the value of A varies between 0.65 and 0.85.[17] Additionally, the Zener–Holloman parameter (Z) is calculated with Eq. (3).[17]

The importance of temperature (T) in the kinetics of the transformation is expressed in the Zener–Holloman parameter (Z) in Eq. (3).[17] It has been previously

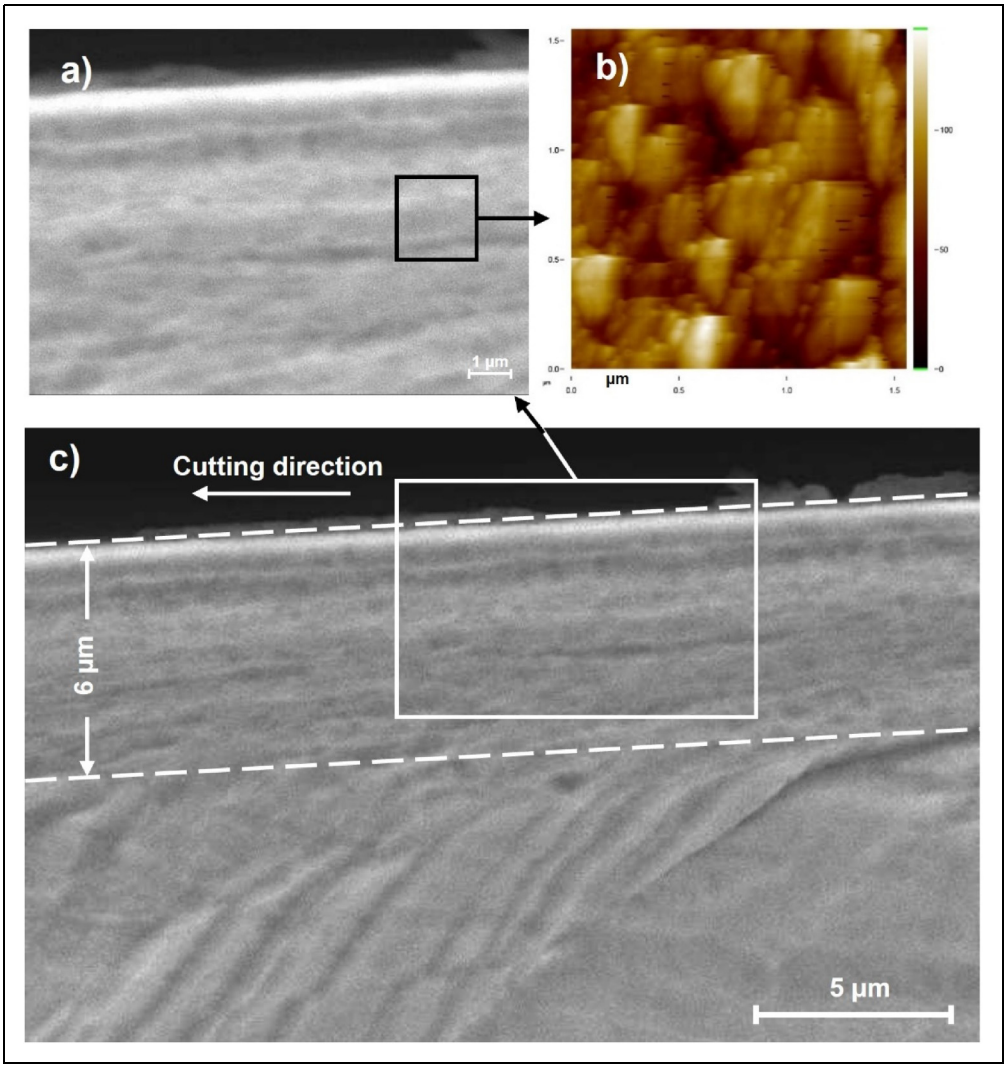

Figure 6. The featureless SPD layer: (a) detail SEM image, (b) detail AFM image, and (c) SEM image.

explained in the literature that the thermal activation energy required for DRX is provided by the heat energy produced in the cutting process and that the plastic deformation and cutting temperature in machining are high enough to initiate the grain refinement process.[4]

$$f(\sigma_p) = Z = \dot{\varepsilon} \exp\left(\frac{Q}{RT}\right) \tag{3}$$

where $\dot{\varepsilon}$ is the strain rate, R is the gas constant (8.32 kJ/(mol·K)), T is the deformation temperature (K), Q is the activation energy for the DRX, and $f(\sigma_p)$ is the stress function and the right side of the equation is denoted as the Zener–Hollomon parameter (Z).[11,16,17]

In addition, the actual cutting temperatures resulting from machining at feedrates of 0.1 mm/rev and 0.5 mm/rev, as well as at a high cutting speed of 300 m/min, are thought to be higher than the measured values (304 °C and 346 °C, respectively, in Figure 4). Because it has been reported in the literature that an interface temperature of 938 °C was measured during the machining of AISI 304 austenitic stainless steel material under dry cutting conditions, at a cutting speed of 180 m/min and a feedrate of 0.16 mm/rev.[38] Since it is difficult to measure the maximum temperature between the cutting tool and the chip during the turning process, in this study, the maximum temperature of the newly formed chip in the cutting zone was measured, as in the literature.[23] On the other hand, it is estimated that the high energy stored on the machined surface during the machining process significantly reduces the recrystallization temperature of the material. As a result, the local heat on the machined surface, which is thought to provide the recrystallization temperature of the AISI 316LVM alloy, caused the DRX, which induced the formation of nanocrystalline grains, as shown in Figure 6(b).

On the other hand, in the SEM images presented in Figure 7, recrystallization formations were observed in some grains, twins, and grain boundaries below the SPD layer as a result of SPD induced by machining performed at a cutting speed of 300 m/min and a feedrate of 0.5 mm/rev under cryogenic cooling. The average size of these formations, which generally occur inside the grains and are estimated to be subgrains, has been

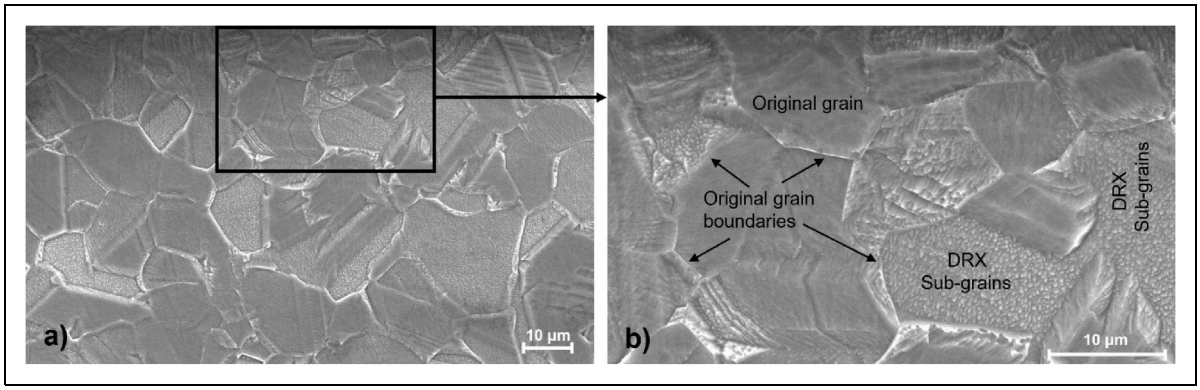

Figure 7. SEM images of CDRX formation in AISI 316LVM material: (a) microstructure detail (average subgrain size 380 nm) and (b) general microstructure.

determined to be 380 nm. While it is estimated that these formations, which have a different appearance from the SPD layer, occur as a result of CDRX,[2,14] the possible DRX mechanism is thought to occur as follows: The existing annealing twin boundaries in the microstructure lose their twin relationship and turn into high-angle boundaries. On the other hand, new grains are formed through progressive lattice rotation at high-angle boundaries and micro shear bands. The recrystallized grains spread homogeneously to the remaining part of the initial grain with progressive deformation, exhibiting a different behavior from the two-stage classical recrystallization process, which includes nucleation and growth stages.[15]

Phase analysis

Deformation-induced martensite formation is a widely known phase transformation in austenitic stainless steels. It has been explained in the literature that plastic deformation, especially at low temperatures, causes austenite–martensite transformation in the structure of austenitic stainless steels. It has been explained in the literature that plastic deformation, especially at low temperatures, causes austenite–martensite transformation in the structure of austenitic stainless steels.[30] The deformation process causes two types of martensitic transformation in austenitic stainless steels with a completely FCC structure: paramagnetic ϵ martensite in the hexagonal close-packed (HCP) crystal structure and ferromagnetic α' martensite in the body-centered cubic (BCC) crystal structure.[39] On the other hand, martensite transformation (ε and α') in austenitic steels depends on the steel composition and SFE, as well as processing parameters such as stress state, temperature, and strain rate.[40]

As seen in the XRD graphs of the surface layers of the machined samples exposed to SPD in Figure 8, no martensite peaks indicating phase transformation were found in this study. This can be explained by taking into account the chemical composition of the workpiece material, SFE value, and deformation temperature. The *SFE* value of a metallic alloy largely depends on the alloying elements and deformation temperature.[41,42] The relationship of chemical composition to SFE is expressed below by Schram and Reed in Eq. (4).[43]

$$\begin{aligned}\mathrm{SFE(mJ/m^2)} = {} & 6.2(\%\mathrm{Ni}) + 9.3(\%\mathrm{Mo}) \\ & + 3.2(\%\mathrm{Mn}) + 0.7(\%\mathrm{Cr}) - 53 \end{aligned} \quad (4)$$

The SFE is an important factor affecting martensitic transformation. The deformation causes austenite–martensite phase transformation in alloys with low SFE values (<20 $\mathrm{mJ/m^2}$), twinning in alloys with medium SFE values (20–45 $\mathrm{mJ/m^2}$), and dislocation slip in alloys with high SFE values (> 45 $\mathrm{mJ/m^2}$).[41,42,44] It was determined using Eq. 4 that the AISI 316LVM alloy machined in this study had a high SFE value of 81.7 $\mathrm{mJ/m^2}$. Therefore, as stated by Yusuf et al.,[41] it was concluded that martensitic transformation can be suppressed in austenitic steels subjected to SPD in the case of alloys with high SFE and medium to high cutting temperatures.

However, a $M_{d(30/50)}$ temperature limit has been reported in the literature where austenite–martensite transformation cannot occur under deformation.[40,44] Martensitic transformation is not expected in deformations above this specified $M_{d(30/50)}$ temperature. The dependence of temperature on material composition for different steels is formulated in Eq. (5).[40] The $M_{d(30/50)}$ is the temperature at which 50% α' martensite is formed with 30% real deformation under tensile conditions.

$$\begin{aligned} M_{d(30/50)}(^\circ\mathrm{C}) = {} & 413 - 462(\%[\mathrm{C}+\mathrm{N}]) \\ & - 18.5(\%\mathrm{Mo}) - 13.7(\%\mathrm{Cr}) \\ & - 9.5(\%\mathrm{Ni}) - 9.2(\%\mathrm{Si}) \\ & - 8.1(\%\mathrm{Mn}) \end{aligned} \quad (5)$$

The $M_{d(30/50)}$ temperature of the AISI 316LVM material used in this study, calculated according to Eq. (5), is −78.4 °C. Despite cryogenic cooling, the cutting temperatures during machining were measured at 304 °C for a feedrate of 0.1 mm/rev and 346 °C for a feedrate of 0.5 mm/rev (Figure 4). In addition, both the measured

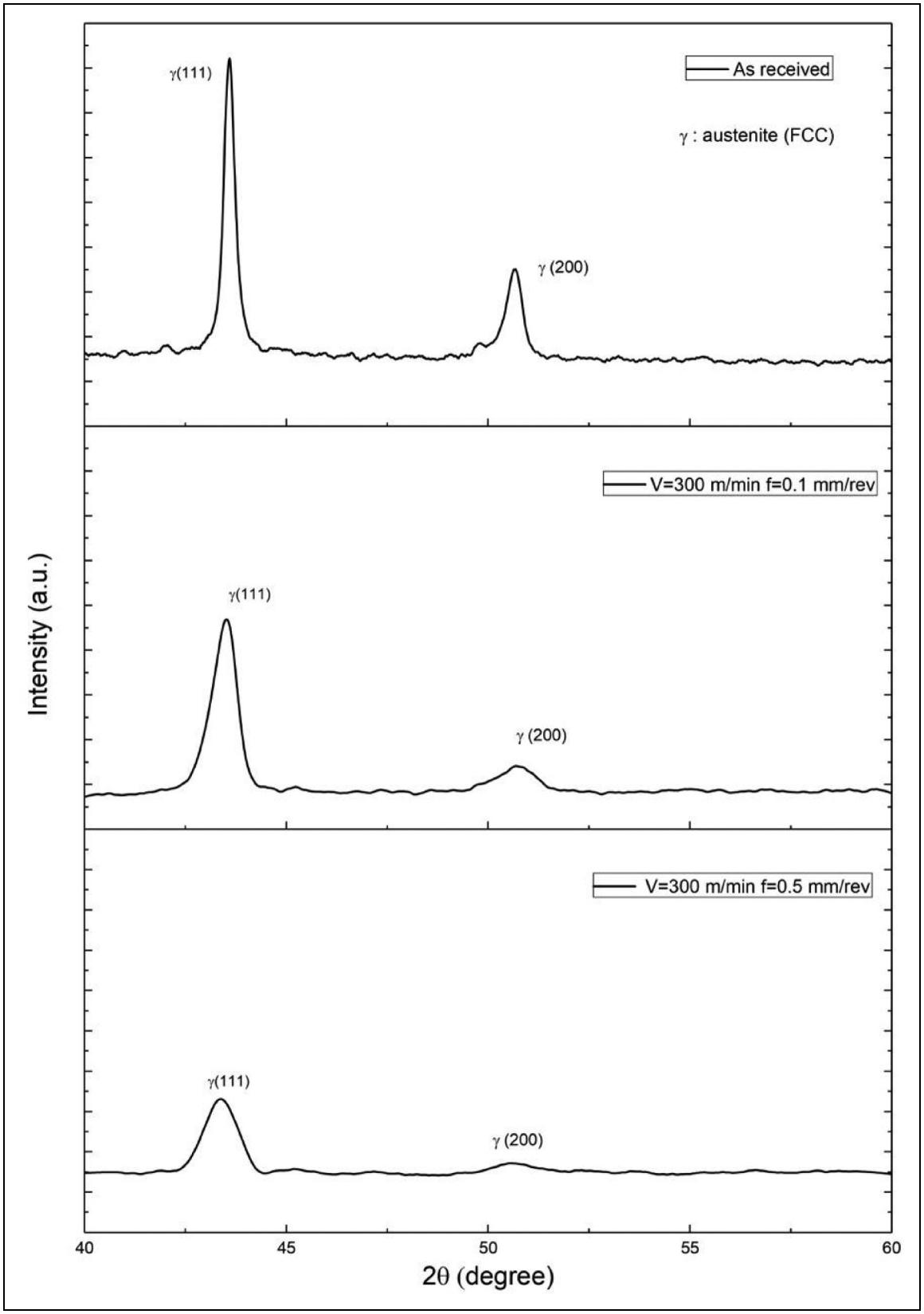

Figure 8. XRD patterns of AISI 316LVM samples.

temperatures and the actual temperatures thought to occur between the cutting tool and the workpiece are considerably higher than the calculated $M_{d(30/50)}$ temperature. Scheriau et al.,[36] who applied a high-pressure torsion process to high SFE 316L alloy at temperatures of −196 °C, 20 °C, and 450 °C, explained the effect of deformation temperature on phase transformation as follows. FCC austenite and HCP ϵ-martensite phase transformation were

observed in the material after the high-pressure torsion process applied at cryogenic temperature (−196 °C). However, only the austenite phase was observed in the diffraction patterns of the samples deformed at 20 °C and 450 °C. In addition, compared to other austenitic stainless steels, 316L, and 316LVM materials are not prone to deformation-induced martensitic phase transformation since they have a more stable phase due to the presence of high molybdenum.[45] In this study, considering the calculated $M_{d(30/50)}$ temperature and the XRD results in Figure 8, it can be said that no austenite–martensite transformation occurs in the ultra grain refinement mechanism. Similar results, where martensitic transformation does not occur in the nanocrystallization mechanism, have been reported in the literature for 316L material applied to warm multi-axial forging[44] and high-pressure torsion processes.[41]

It is thought that the absence of martensitic phase transformation in the nanocrystalline surface layer will positively affect the fatigue and corrosion resistance of medical implants. The effects of possible martensitic phase transformation in the surface layer of austenitic stainless steels due to SPD were explained in a previous study by De Oliveira Silva et al.,[30] as follows. Shrinkage in the microstructure caused by the martensitic phase makes austenitic stainless steel more vulnerable to corrosion. The martensitic transformation causes the passive film to rupture and the corrosion resistance to decrease due to the high defect density in the microstructure. In addition, possible phase transformation on the surface causes residual stresses or galvanic effects due to the presence of two different phases (austenite and martensite).

Nanocrystalization and work-hardening analyses by XRD

As seen in Figure 8, the SPD induced by cryogenic machining in this study caused peak broadening in the XRD patterns of the machined surface of AISI 316LVM material. Because, as explained in the literature, deformation disrupts the regular crystal structure of metallic materials, causing a decrease in peak intensity and peak broadening in the XRD pattern.[46] From the graph presented in Figure 9, it can be seen that there is a correlation between full width at half maximum (FWHM*)* and grain size. Grain size decreased with increasing peak half-width. In response to the 338% broadening of the (1 1 1) peak, the grain size on the machined surface decreased from micron to nano. From the AFM image in Figure 6(b) of the sample machined at a feedrate of 0.5 mm/rev, it was determined that the grain size of the featureless layer in the subsurface was 93 nm. Compared to the 16.8 μm average grain size of the as-received material, significant SPD-induced grain refinement occurred in the subsurface layer. Consistent with the alteration in microstructure, peak broadening has been reported to result from the combined effect of grain size reduction and dislocation density increase.[8,47]

On the other hand, grain size and work-hardening are important factors affecting the hardness of a material. Thermomechanical effects occurring in machining processes cause grain refinement in the subsurface layer of the machined materials as well as work-hardening.[4,7,33,48] The SPD layer formed in the subsurface of the samples subjected to the machining process is also called the work-hardening layer.[33,48] Generally, an increase in microhardness occurs in the SPD layer formed as a result of plastic deformation.[33] Because austenitic stainless steels are materials that are very sensitive to strain, high strain rates, and work-hardening.[49]

It has been reported in the literature that the level of work-hardening can be estimated from the peak broadening in the XRD pattern of the materials.[6,7] Compared to the FWHM and microhardness values of the as-received material in Supplementary Figure S1, the high FWHM and microhardness values of the machined samples are evidence of the significant hardening of the surface and subsurface layer after cryogenic machining. As seen in Supplementary Figure S1, work-hardening (peak breadth) and microhardness lines have a similar tendency. With the FWHM values increasing with the feedrate, work-hardening occurred at rates of 169% and 338% in the subsurface layers for 0.1 mm/rev and 0.5 mm/rev feedrates, respectively, while the hardness increased by 71% and 115%, respectively. It is thought that the high strain rate caused by the high cutting speed of 300 m/min causes the microhardness to increase by increasing the work-hardening (strain hardening) exponent of the material.[50] In addition, the high pressure between the tool and the workpiece induced by the radial cutting force (Figure 4) increasing with the feedrate caused an increase in thermomechanical loads, a deformed layer, and work-hardening on the machined surface, as previously reported by Klocke et al.[4] It has been previously reported by Eziarslan et al.[48] that this situation increases the microhardness by increasing dislocation accumulation just below the machined surface. In addition, work-hardening resulting from chip contraction, which increases with the feedrate, causes an increase in microhardness. On the other hand, as reported in previous studies, the ploughing effect of the cutting tool on the machined surface, which was exposed to significant nose wear (Figure 5) at a high feedrate (0.5 mm/rev), also caused compression of the material on the machined surface, deeper plastic deformation and higher work-hardening.[4,7]

In addition to all these, the dominant work-hardening effect, which occurs as a result of cryogenic cooling reducing the effect of thermal softening by reducing the cutting temperature and making machining difficult, increased the hardness of the subsurface layer. Because it is estimated that dislocation movements underlie the hardening and thermal softening mechanisms that occur during the machining process. Dislocations whose ability to move is reduced or blocked as a result of low temperatures cause the force required for plastic deformation to increase and therefore the material to become harder and with higher strength.[37]

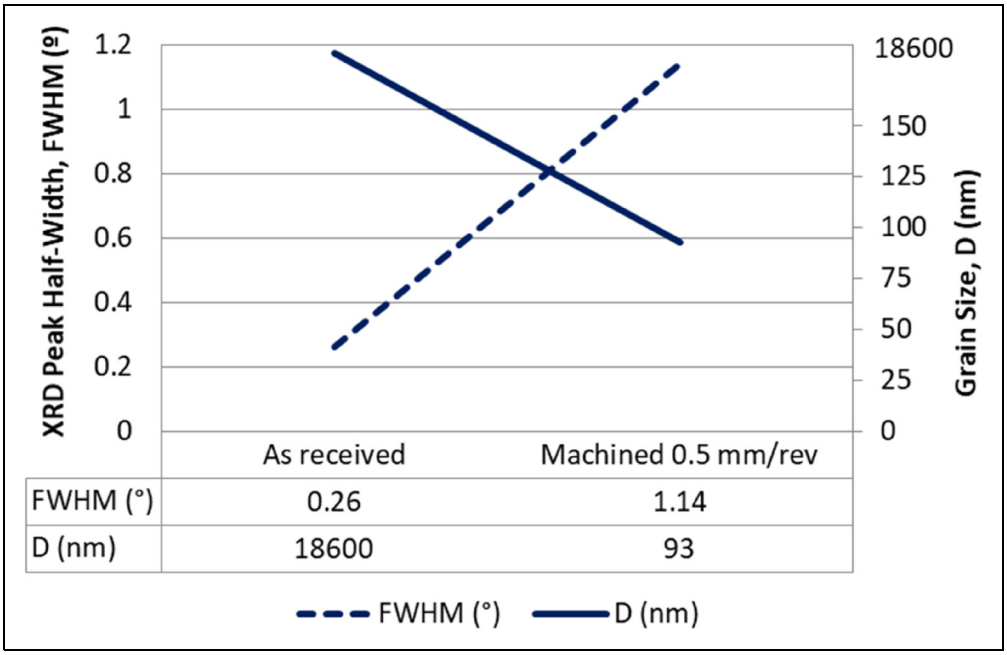

Figure 9. Full width at half maximum (FWHM) of (1 1 1) peaks and grain size of the sample.

On the other hand, the effect of microstructural alteration on hardness should not be ignored. As seen in Supplementary Figure S2, there is a correlation between grain size and hardness due to decreasing grain size and increasing hardness. The SPD caused an increase in hardness in response to ultra-fine grain refinement in the subsurface layer. The relationship between grain size and microhardness follows the classical Hall–Petch line.[37] Compared to the 240 HV microhardness of the as-received material, the microhardness in the subsurface layer of the machined sample increased by 115% to 516 HV. Similarly, the dramatic increase in hardness after significant grain refinment in machining has been reported many times in the literature.[4,7,13,14,32]

In addition to the above explanations, it can be said that cryogenic cooling and high strain rate in this study are effective on grain refinement in the subsurface layer as well as work-hardening. Because in the DRX process, grain size is limited by intragranular work-hardening. More hardening occurs at low temperatures and high strain rates (i.e., high Zener–Holloman values, Z). Because very high heat absorption from the cutting zone with cryogenic cooling causes the onset of the DRX to be delayed and a high Zener–Holloman (Z) value according to Eq. (3). In addition, the strain rate increasing with high feedrate and high cutting speed also causes high Zener–Holloman (Z) value according to Eq. (3). The average grain size (D_{DRX}) in the dynamic crystallized structure is a function of the Zener–Holloman parameter as expressed in Eq. (6).[10,11] It is understood from Eq. (6) that the DRX microstructure of the sample deformed under a high Zener–Holloman (Z) value will be finer compared to the sample deformed under a low Z value.[11] As a result, the 115% microhardness increase observed in the subsurface layer of the sample machined under aggressive cutting condition such as high cutting speed of 300 m/min, high feedrate of 0.5 mm/rev and cryogenic LN_2 cooling is attributed to the combined effect of surface integrity characterizations such as work-hardening and grain refinement.[4,7]

$$Z \cdot D_{\mathrm{DRX}}^{m} = A \tag{6}$$

As a result, it can be considered that nanocrystallization and hardness increase in the surface layer can be a powerful tool to improve the mechanical strength, fatigue life, wear resistance, corrosion resistance, and biocompatibility of AISI 316 LVM medical implant alloy.[51,52] The potential of using surface nanocrystallization to reduce corrosion and fatigue failure of metallic implants has been discussed in the literature. Microstructure properties are closely related to the corrosion fatigue strength of biomedical alloys. Since there is a complex interaction between fatigue and corrosion in the physiological environment, plastic deformation, and microstructure have a decisive effect on fatigue crack nucleation and crack growth mechanisms.[51]

Previous studies have reported that SPD-induced surface nanocrystallization significantly improves the biocompatibility,[53,54] fatigue strength,[45,47,51,52,55] corrosion resistance,[5,6,47,51,54,56] and wear resistance[51,52,57] of biomedical implant materials such as austenitic stainless steel alloys, Ti alloys, Co alloys, and Mg alloys. Researchers reported that nanocrystallization reduces the anodic current density and passive current density, increases the corrosion potential, accelerates the formation of the protective passive film and increases pitting corrosion resistance.[6,47,51,52,54,57] In other words, fast, stable, less defective, and better passivation behavior was observed on the fine-grained surface.[6,54] It was also

reported that the reduced grain size after surface nanocrystallization increases mechanical strength while preventing fatigue crack initiation and propagation.[45,47,51,52,55] It has been reported that the nanocrystal structure in the surface layer of AISI 316L stainless steel prevents the initiation of cracks on the surface by preventing the development of shear bands.[52,58] On the other hand, it has been stated that the grain size hardening and deformation hardening in the surface layer will delay the formation of cracks due to the increase in strength, and thus the fatigue strength will be better.[47,52] In addition, it has been reported that the surface hardening induced by nanocrystallization can also improve wear resistance.[45,52] Thus, since a harder surface will increase wear resistance, the possible release of wear debris that may occur on the implant surface surface is prevented or minimized, thus extending the implant service life.[52]

In the literature, the initiation of corrosion fatigue cracks in metallic materials has been associated with the pits formed on the surface due to pitting corrosion and the intergranular corrosion within these pits.[51,59] While coarse austenite grains on the surface reduce pitting corrosion resistance,[54] grain size heterogeneity has the potential to reduce the fatigue strength of alloys. Therefore, it is recommended that microstructural features such as grain refinement and grain size uniformity be carefully controlled to achieve improved corrosion fatigue characteristics in austenitic stainless steels.[51,60]

On the other hand, it has been reported that nanocrystalline surfaces have lower contact angle values and therefore better wettability compared to their coarse-grained counterparts.[54] Since higher wettability can improve cell attachment to the implant, it has been reported that nanocrystallization can improve the adhesion and proliferation of osteoblasts on the 316L implant surface.[52,61] Because nano/ultra-fine particles on the implant surface will create a larger grain boundary area, allowing a large number of osteoblast cells to adhere to the implant surface.[54]

Considering the obtained results and previous research, it is thought that the combined effects of surface nanocrystallization and hardness increase induced by SPD in machining will provide improvement in functional properties such as wear resistance, corrosion resistance, fatigue strength, and biocompatibility of medical implants.

Conclusions

This study presented a fundamental study on microstructure, nanocrystallization, DRX, SFE, phase transformation, work-hardening, and microhardness in the machining of AISI 316LVM austenitic stainless steel, a biomedical material, under aggressive cutting parameters and cryogenic cooling. The results show that cryogenic machining significantly affects the surface integrity characterizations. The key findings from this research study are summarized as follows:

- Under a high cutting speed of 300 m/min and cryogenic LN_2 cooling, it was determined that an approximately 3.5 to 5.5 μm thick SPD layer was formed at a feedrate of 0.1 mm/rev, while an approximately 27 to 38 μm thick SPD layer was formed at a high feedrate of 0.5 mm/rev.
- The SPD induced by a high feedrate (0.5 mm/rev) resulted in a much thicker SPD layer in the subsurface of the machined sample. While the shear bands in the subsurface microstructure increased due to the SPD, the boundaries of the grains elongating in the cutting direction disappeared as they approached the machined surface.
- A featureless layer with a thickness of 6 μm was detected in the subsurface. It was understood from the AFM image that this featureless layer was a nanolayer containing DRX grains with an average size of 93 nm.
- Recrystallization formations with an average size of 380 nm were observed in some grains, twins, and grain boundaries in the microstructure.
- It was concluded that CDRX is the mechanism that causes nanocrystallization in the subsurface and some grains of the AISI 316LVM alloy with high SFE.
- No martensitic phase transformation was found in the surface layer where nanocrystallization occurred.
- The SPD caused the broadening of the peaks in the XRD pattern. While the 338% broadening of the (1 1 1) peak caused the same amount of work-hardening in the subsurface layer, the microhardness increased by 115%, from 240 HV to 516 HV.
- In response to the 338% broadening of the (1 1 1) peak, the grain size in the subsurface of the workpiece decreased from micron to nano.

In addition to all these results, it will be useful to investigate the effects of different cooling conditions, different cutting parameters and different cryogenic cooling techniques on SPD-induced DRX in AISI 316 LVM alloy in the future. In addition, systematic comprehensive studies on the methods of preventing and reducing corrosion fatigue failure of metallic implants are almost non-existent in the literature. Therefore, a systematic investigation of the effects of deformation, nanocrystallization, crystal phase, residual stresses, and surface texture on corrosion, fatigue, wear, and biocompatibility performance in metallic implant alloys will be useful. In addition, it is thought that it will be useful to investigate the effects of crystal phase, grain size, surface texture, microhardness, and residual stresses on fatigue crack initiation and crack propagation mechanisms in metallic implant alloys.

Authors' contribution

All authors contributed to the study conception and design. Material preparation, data collection, and analysis were performed by Emin Ozdemir. The first draft of the manuscript was written by Emin Ozdemir and all authors commented on previous versions of the manuscript. All authors read and approved the final manuscript.

Data availability

Data will be made available on request.

Declaration of conflicting interests

The authors declared no potential conflicts of interest with respect to the research, authorship, and/or publication of this article.

Funding

The authors disclosed receipt of the following financial support for the research, authorship, and/or publication of this article: This work was supported by Gazi University, Department of Scientific Research Projects Coordination Unit (BAP) [project number 18/2016-02].

ORCID iD

Emin Ozdemir https://orcid.org/0000-0002-6517-9270

Supplemental material

Supplemental material for this article is available online.

References

1. Park JB. Metallic biometarials. In: Bronzino JD (ed) *The biomedical fngineering handbook*. 2nd ed. Boca Raton, FL: CRC Press LLC, 2000, pp.IV-1–IV-8.
2. Ozdemir E. Improvement of surface integrity and functional performance in machining process of the austenitic stainless steels used in the biomedical industry. PhD Thesis, Gazi University, Turkiye, 2020.
3. Jawahir IS, Attia H, Biermann D, et al. Cryogenic manufacturing processes. *CIRP Ann* 2016; 65: 713–736.
4. Klocke F, Döbbeler B, Lung S, et al. Analysis of surface integrity in machining of AISI 304 stainless steel under various cooling and cutting conditions. *AIP Conf Proc Palermo, Italy* April 2018; 1960: 1–6.
5. Pu Z, Song GL, Yang S, et al. Grain refined and basal textured surface produced by burnishing for improved corrosion performance of AZ31B Mg alloy. *Corros Sci* 2012; 57: 192–201.
6. Tang J, Luo HY and Zhang YB. Enhancing the surface integrity and corrosion resistance of Ti–6Al–4V titanium alloy through cryogenic burnishing. *J Adv Manuf Technol* 2017; 88: 2785–2793.
7. Pu Z, Outeiro JC, Batista AC, et al. Enhanced surface integrity of AZ31B Mg alloy by cryogenic machining towards improved functional performance of machined components. *Int J Mach Tools Manuf* 2012; 56: 17–27.
8. Yang S, Puleo DA, Dillon Jr OW, et al. Surface layer modifications in Co–Cr–Mo biomedical alloy from cryogenic burnishing. *Proc Eng* 2011; 19: 383–388.
9. Meyers MA, LaSalvia JC, Nestorenko VF, et al. Dynamic recrystallization in high strain rate deformation. *Proc Third Int Conf Recrystal Rel Phen* 1997: 279–286.
10. Wang X, Wang D, Jin J, et al. Effects of strain rates and twins evolution on dynamic recrystallization mechanisms of austenite stainless steel. *Mater Sci Eng A* 2019; 761: 138044.
11. Dehghan-Manshadi A, Barnett MR and Hodgson PD. Recrystallization in AISI 304 austenitic stainless steel during and after hot deformation. *Mater Sci Eng A* 2008; 485: 664–672.
12. Musin F, Belyakov A, Kaibyshev R, et al. Microstructure evolution in a cast 1421Al alloy during hot equal-channel angular extrusion. *Rev Adv Mater Sci* 2010; 25: 107–112.
13. Ni H, Elmadagli M and Alpas AT. Mechanical properties and microstructures of 1100 aluminum subjected to dry machining. *Mater Sci Eng A* 2004; 385: 267–278.
14. Wusatowska-Sarnek AM, Dubiel B, Czyrska-Filemonowicz A, et al. Microstructural characterization of the white etching layer in nickel-based superalloy. *Metall Mat Trans A* 2011; 42: 3813–3825.
15. Huang K and Loge REA. Review of dynamic recrystallization phenomena in metallic materials. *Mater Des* 2016; 111: 548–574.
16. Sakai T, Belyakov A, Kaibyshev R, et al. Dynamic and post-dynamic recrystallization under hot, cold and severe plastic deformation conditions. *Progr Mater Sci* 2014; 60: 130–207.
17. Fernandez AI, Uranga P, Lopez B, et al. Dynamic recrystallization behavior covering a wide austenite grain size range in Nb and Nb–Ti microalloyed steels. *Mater Sci Eng A* 2003; 361: 367–376.
18. Khanna N, Agrawal C, Pimenov DY, et al. Review on design and development of cryogenic machining setups for heat resistant alloys and composites. *J Manuf Processes* 2011; 68: 398–422.
19. Saha P, Narain R, Kumar R, et al. Cryogenics as a cleaner cooling strategy for machining applications: a concise review. *Int J Energy Clean Environ* 2022; 23: 129–141.
20. UGITECH. *Material inspection certificate, ASTM F 138/13 (AISI 316 LVM)*. Ugine, France, 2015.
21. ASTM-E112:2004. Standard test methods for determining average grain size.
22. SECO. Catalog and technical guide 2015, turning. 2015.
23. Ozdemir E and Gullu A. Investigation of the surface quality and machinability of AISI 316LVM. *Proc Inst Mech Eng Part E: J Process Mech Eng* 2023: 095440892 31190764.
24. Fernández-Abia AI, Barreiro J, López de Lacalle LN, et al. Behavior of austenitic stainless steels at high speed turning using specific force coefficients. *Int J Adv Manuf Technol* 2012; 62: 505–515.
25. Lin HM. The study of high speed fine turning of austenitic stainless steel. *J Arch Mater Manuf Eng* 2008; 2008: 191–194.
26. Mashinini PM, Soni H and Gupta K. Investigation on dry machining of stainless steel 316 using textured tungsten carbide tools. *Mater Res Express* 2019; 7: 016502.
27. Du H, Karasev A, Björk T, et al. Assessment of chip breakability during turning of stainless steels based on weight distributions of chips. *Metals (Basel)* 2020; 10: 675.
28. Korkut I, Kasap M, Ciftci I, et al. Determination of optimum cutting parameters during machining of AISI 304 austenitic stainless steel. *Mater Des* 2004; 25: 303–305.
29. Özbek NA, Çiçek A, Gülesin M, et al. Effect of cutting conditions on wear performance of cryogenically treated tungsten carbide inserts in dry turning of stainless steel. *Tribol Int* 2016; 94: 223–233.
30. De Oliveira Silva PM, De Abreu HFG, De Albuquerque VHC, et al. Cold deformation effect on the microstructures and mechanical properties of AISI 301LN and 316L stainless steels. *Mater Des* 2011; 32: 605–614.
31. De Abreu HFG, De Carvalho SS, Lima-Neto D, et al. Deformation induced martensite in an AISI 301LN stainless

steel: characterization and influence on pitting corrosion resistance. *Mater Res* 2007; 10: 359–366.
32. Umbrello D. Investigation of surface integrity in dry machining of Inconel 718. *J Adv Manuf Technol* 2013; 69: 2183–2190.
33. Yazid MZA, CheHaron CH, Ghani JA, et al. Surface integrity of inconel 718 when finish turning with PVD coated carbide tool under MQL. *Proc Eng* 2011; 19: 396–401.
34. Lee WS, Chen TH, Lin CF, et al. Dynamic mechanical response of biomedical 316L stainless steel as function of strain rate and temperature. *Bioinorg Chem App* 2011; 2011: 173782.
35. Pang CH, Hing P and See A. Application of phase-imaging tapping-mode atomic-force microscopy to investigate the grain growth and surface morphology of TiSi 2. *J Vac Sci Technol B* 2002; 20: 1866–1869.
36. Scheriau S, Zhang Z, Kleber S, et al. Deformation mechanisms of a modified 316L austenitic steel subjected to high-pressure torsion. *Mater Sci Eng A* 2011; 528: 2776–2786.
37. Callister WD and Rethwisch DG. *Material science and engineering*. 9th ed. New York: Wiley, 2014.
38. Kulkarni A, Sargade V and More C. Machinability investigation of AISI 304 austenitic stainless steels using multilayer AlTiN/TiAlN coated carbide inserts. *Proc Manuf* 2018; 20: 548–553.
39. Altenberger I, Scholtes B, Martin U, et al. Cyclic deformation and near surface microstructures of shot peened or deep rolled austenitic stainless steel AISI 304. *Mater Sci Eng A* 1999; 264: 1–16.
40. Padilha AF and Rios PR. Decomposition of austenite in austenitic stainless steel. *ISIJ Int* 2002; 42: 325–337.
41. Yusuf SM, Chen Y, Yang S, et al. Microstructural evolution and strengthening of selective laser melted 316L stainless steel processed by high-pressure torsion. *Mater Charact* 2020; 159: 110012.
42. Lu J, Hultman L, Holmström E, et al. Stacking fault energies in austenitic stainless steels. *Acta Mater* 2016; 111: 39–46.
43. Schram RE and Reed RP. Stacking fault energies of seven commercial austenitic stainless steels. *Metall Trans A* 1975; 6: 1345–1351.
44. Muley SV, Vidvans AN, Chaudhari GP, et al. An assessment of ultra fine grained 316L stainless steel for implant applications. *Acta Biomater* 2016; 30: 408–419.
45. Roland T, Retraint D, Lu K, et al. Enhanced mechanical behavior of a nanocrystallised stainless steel and its thermal stability. *Mater Sci Eng A* 2007; 445: 281–288.
46. Çörekçi S, Dugan S, Öztürk MK, et al. Characterization of AlInN/AlN/GaN heterostructures with different AlN buffer thickness. *J Electron Mater* 2016; 45: 3278–3284.
47. Jiang XP, Wang XY, Li JX, et al. Enhancement of fatigue and corrosion properties of pure Ti by sandblasting. *Mater Sci Eng A* 2006; 429: 30–35.
48. Ezilarasan C, Senthil-Kumar VS and Velayudham A. Effect of machining parameters on surface integrity in machining nimonic C-263 super alloy using whisker-reinforced ceramic insert. *J Mater Eng Perform* 2013; 22: 1619–1628.
49. Outeiro JC, Umbrello D and M'Saoubi R. Experimental and numerical modelling of the residual stresses induced in orthogonal cutting of AISI 316L steel. *Int J Mach Tools Manuf* 2006; 46: 1786–1794.
50. Tang C, Zhu J and Zhang Y. Effect of strain rate (ε̇) on strain hardening exponent n of some metallic materials. *Acta Metallurg Sin (Engl Lett)* 1994; 7: 183–186.
51. Antunes RA and De Oliveira MCL. Corrosion fatigue of biomedical metallic alloys: mechanisms and mitigation. *Acta Biomater* 2012; 8: 937–962.
52. Acharya S, Suwas S and Chatterjee K. Review of recent developments in surface nanocrystallization of metallic biomaterials. *Nanoscale* 2021; 13: 2286–2301.
53. Kim TN, Balakrishnan A, Lee BC, et al. In vitro fibroblast response to ultra fine grained titanium produced by a severe plastic deformation process. *J Mater Sci: Mater Med* 2008; 19: 553–557.
54. Prakash NS, Mandal S, Chakrabarti D, et al. Unraveling the effects of nano-grained microstructure on mechanical behavior, corrosion, and in vitro biocompatibility of 316L austenitic stainless steel. *Mater Chem Phys* 2024; 318: 129292.
55. Roland T, Retraint D, Lu K, et al. Fatigue life improvement through surface nanostructuring of stainless steel by means of surface mechanical attrition treatment. *Scr Mater* 2006; 54: 1949–1954.
56. Di Schino A and Kenny JM. Effects of the grain size on the corrosion behavior of refined AISI 304 austenitic stainless steels. *J Mater Sci Lett* 2002; 21: 1631–1634.
57. Sun HQ, Shi YN and Zhang MX. Wear behaviour of AZ91D magnesium alloy with a nanocrystalline surface layer. *Surf Coatings Technol* 2008; 202: 2859–2864.
58. Bahl S, Suwas S and Chatterjee K. Comprehensive review on alloy design, processing, and performance of β Titanium alloys as biomedical materials. *Int Mater Rev* 2021; 66: 114–139.
59. Xie J, Alpas AT and Northwood DO. A mechanism for the crack initiation of corrosion fatigue of Type 316L stainless steel in Hank's solution. *Mater Charact* 2002; 48: 271–277.
60. Swarts E, Kop A, Jones N, et al. Microstructural features in fractured high nitrogen stainless steel hip prostheses: a retrieval study of polished, tapered femoral stems. *J Biomed Mater Res A* 2008; 84: 753–760.
61. Bahl S, Shreyas P, Trishul MA, et al. Enhancing the mechanical and biological performance of a metallic biomaterial for orthopedic applications through changes in the surface oxide layer by nanocrystalline surface modification. *Nanoscale* 2015; 7: 7704–7716.